AGU PUBLICATIONS

JGR

Journal of Geophysical Research: Oceans

RESEARCH ARTICLE

10.1002/2016JC012666

Key Points:
- Within isopycnal layers dissipation varies by at least 2 orders of magnitude in the Solomon Sea
- Dissipation is maximum in the surface and decreases by 2–3 orders of magnitude by 2000 m depth
- Dissipation is seasonally variable, particularly in the thermocline

Correspondence to:
M. S. Alberty,
malberty@ucsd.edu

Citation:
Alberty, M. S., J. Sprintall, J. MacKinnon, A. Ganachaud, S. Cravatte, G. Eldin, C. Germineaud, and A. Melet (2017), Spatial patterns of mixing in the Solomon Sea, *J. Geophys. Res. Oceans*, *122*, 4021–4039, doi:10.1002/2016JC012666.

Received 17 JAN 2017
Accepted 19 APR 2017
Accepted article online 25 APR 2017
Published online 15 MAY 2017

Spatial patterns of mixing in the Solomon Sea

M. S. Alberty[1], J. Sprintall[1], J. MacKinnon[1], A. Ganachaud[2], S. Cravatte[2], G. Eldin[2], C. Germineaud[2], and A. Melet[3]

[1]Scripps Institution of Oceanography, University of California, San Diego, La Jolla, California, USA, [2]Laboratoire d'Etudes en Géophysique et Océanographie Spatiales, Université de Toulouse, CNES, CNRS, IRD, UPS, Toulouse, France, [3]Mercator Ocean, Ramonville Saint-Agne, France

Abstract The Solomon Sea is a marginal sea in the southwest Pacific that connects subtropical and equatorial circulation, constricting transport of South Pacific Subtropical Mode Water and Antarctic Intermediate Water through its deep, narrow channels. Marginal sea topography inhibits internal waves from propagating out and into the open ocean, making these regions hot spots for energy dissipation and mixing. Data from two hydrographic cruises and from Argo profiles are employed to indirectly infer mixing from observations for the first time in the Solomon Sea. Thorpe and finescale methods indirectly estimate the rate of dissipation of kinetic energy (ϵ) and indicate that it is maximum in the surface and thermocline layers and decreases by 2–3 orders of magnitude by 2000 m depth. Estimates of diapycnal diffusivity from the observations and a simple diffusive model agree in magnitude but have different depth structures, likely reflecting the combined influence of both diapycnal mixing and isopycnal stirring. Spatial variability of ϵ is large, spanning at least 2 orders of magnitude within isopycnal layers. Seasonal variability of ϵ reflects regional monsoonal changes in large-scale oceanic and atmospheric conditions with ϵ increased in July and decreased in March. Finally, tide power input and topographic roughness are well correlated with mean spatial patterns of mixing within intermediate and deep isopycnals but are not clearly correlated with thermocline mixing patterns.

Plain Language Summary In the ocean, a number of physical processes move heat, salt, and nutrients around vertically by mixing neighboring layers of the ocean together. This study investigates the strength and spatial patterns of this mixing in the Solomon Sea, which is located in the tropical west Pacific Ocean. Estimates of the strength of mixing are made using measurements of temperature, salinity, and velocity taken during two scientific cruises in the Solomon Sea. Measurements of temperature and salinity from a network of floats that move up and down through the ocean and travel with ocean currents were also used to estimate the strength and patterns of mixing. This research finds three key results for mixing in the Solomon Sea: (1) Mixing is strongest near the surface of the Solomon Sea and less strong at deeper depths. (2) Mixing varies horizontally, with stronger mixing above underwater ridges and seamounts, and with weaker mixing above smooth and flat seafloor. (3) The strength of mixing changes with the seasons, possibly related to the monsoonal winds which also change in strength over the seasons.

1. Introduction

Marginal seas have long been identified as regions that contribute significantly to kinetic energy dissipation and water mass modification [*Munk and Wunsch*, 1998; *Price and Yang*, 1998; *Egbert and Ray*, 2000]. These seas are almost entirely separated from the open ocean by topographic boundaries, save for a few straits or channels which allow the exchange of water masses between the marginal seas and the open ocean. Tidal currents, enhanced by the topographic constrictions, pass over topography at the exchange points and generate internal waves. The propagation and spreading of the internal wave energy may be restricted by the islands and sills bounding the sea, leading to enhanced dissipation and mixing within the marginal sea and along the boundaries [*St Laurent*, 2008]. The topographic properties of marginal seas make them unique regions of concentrated water mass modification, where water properties are transformed by lateral stirring and vertical mixing. In the South China Sea, for example, tidal flows through Luzon Strait produce

energetic internal waves and strong turbulence throughout the region [*St Laurent*, 2008; *Alford et al.*, 2011, 2015].

The Solomon Sea is a marginal sea located in the equatorial Southwest Pacific that is important for tropical circulation and climate [*Ganachaud et al.*, 2014]. The Solomon Sea is bordered by the main island of Papua New Guinea to the west, the islands New Britain and New Ireland of Papua New Guinea to the north, and the Solomon Islands to the east (Figure 1a). South Pacific Subtropical Mode Water (STMW, $23.3 < \sigma_\theta < 26.7$) and Antarctic Intermediate Water (AAIW, $26.7 < \sigma_\theta < 27.5$) enter through the southern opening of the Solomon Sea with a total transport of about 26 ± 7 Sv (Figure 1b) [*Fine et al.*, 1994; *Davis et al.*, 2012; *Gasparin et al.*, 2012; *Zilberman et al.*, 2013; *Germineaud et al.*, 2016]. The island chains constrain

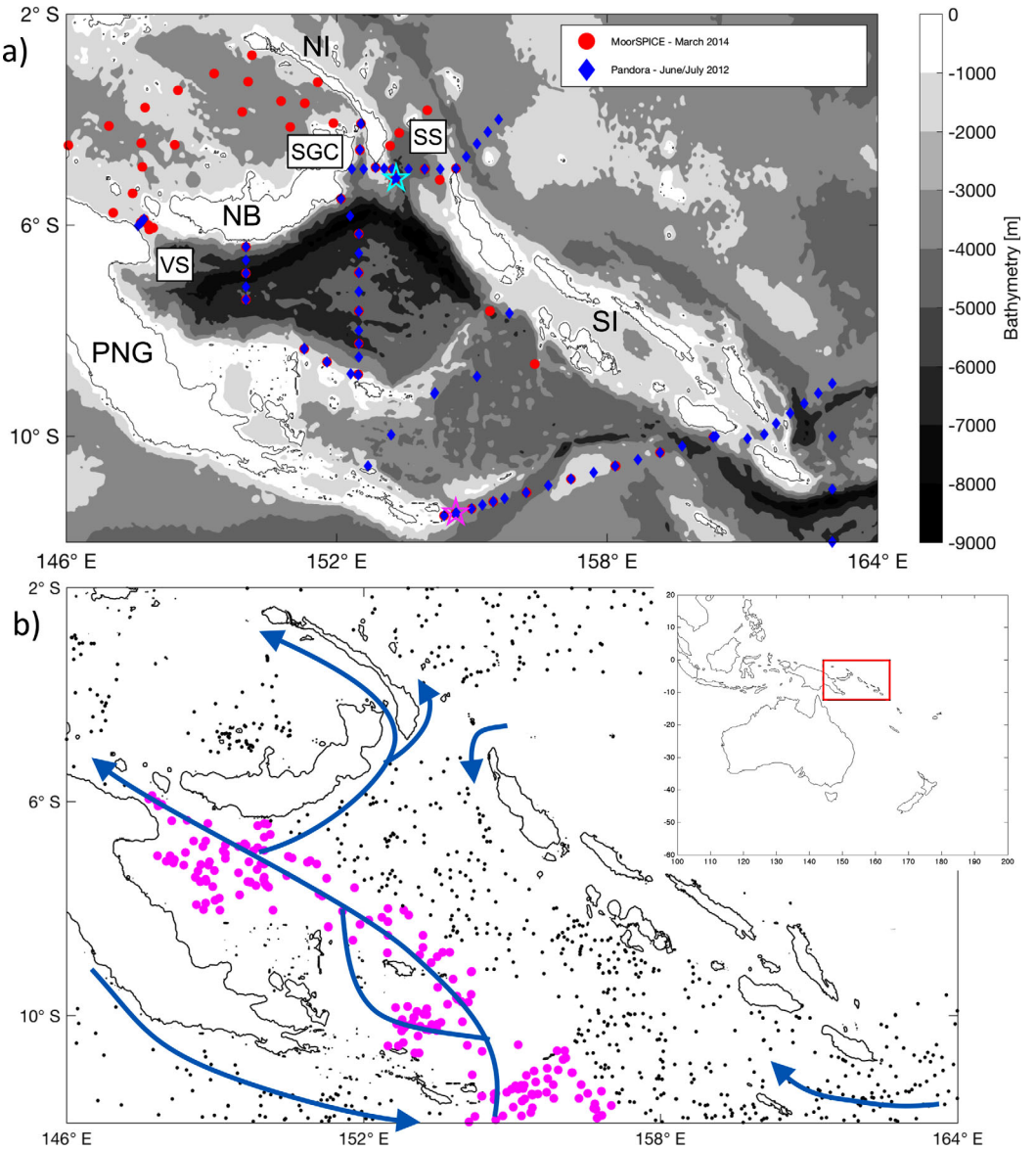

Figure 1. (a) Map of Solomon Sea bathymetry including the main island of Papua New Guinea (PNG), New Britain (NB), New Ireland (NI), and the Solomon Islands (SI). The primary outflow channels, Vitiaz Strait (VS), St. George Channel (SGC), and Solomon Strait (SS), are noted. Red circles indicate CTD/LADCP cast locations for the MoorSPICE cruise (March 2014) while blue diamonds indicate cast locations for the Pandora cruise (June/July 2012). The cyan and magenta stars are the locations of Pandora station 42 and MoorSPICE station 50, respectively, which are referenced in Figure 5. (b) The locations of the Argo and shipboard observations used to determine profiles of along-path mean diffusivity which are referenced in Figure 7 are shown as magenta dots and all other Argo observations shown as black dots. Blue lines are a schematic representation of the New Guinea Coastal Current/New Guinea Coastal Undercurrent (NGCC/NGCU) system that traverses the basin. The red box in the inset map indicates the location of the primary map within the Southwest Pacific.

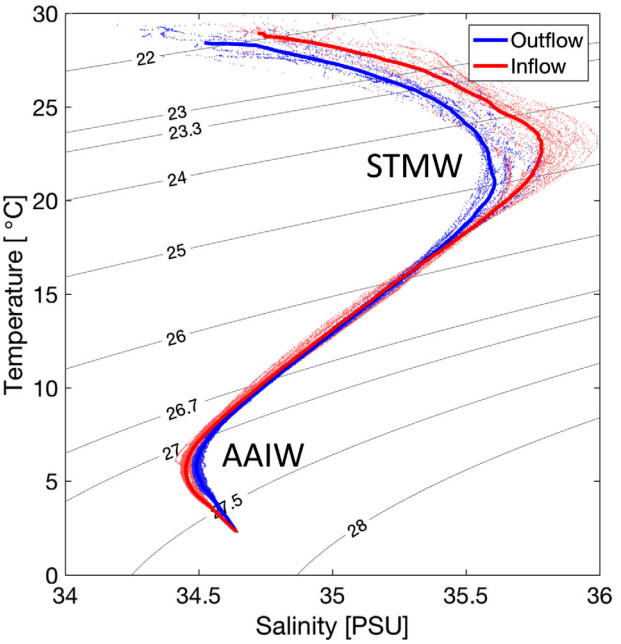

Figure 2. Mean temperature-salinity relationship of the Solomon Sea water mass inflow region (13°S–11°S, 153°E–156°E, red line) and outflow region north of Vitiaz Strait (7°S–4°S, 146°E–148°E, blue line) from Argo profiles. Individual observations are small dots in the corresponding color. STMW is indicated at the salinity maximum in the thermocline layer ($23.3 < \sigma_\theta < 26.7$) and AAIW is identified at the deep salinity minimum in the intermediate layer ($26.7 < \sigma_\theta < 27.5$).

transport such that nearly all of the flow out of the Solomon Sea is accounted for in three relatively deep channels; Vitiaz Strait, St. Georges Channel, and Solomon Strait [*Lindstrom et al*., 1990; *Murray et al*., 1995; *Melet et al*., 2010a; *Cravatte et al*., 2011].

Along the pathways through the Solomon Sea, the AAIW and STMW water masses undergo modification, characterized by a cooling (∼0.5°C) and freshening (∼0.2 PSU) of the STMW, and a warming (∼0.2°C) and an increase in salinity (∼0.04 PSU) of the AAIW along core isopycnals (Figure 2) [*Germineaud et al*., 2016]. Modeled power input into the internal wavefield from the tides shows elevated baroclinic tide generation above ridges in Solomon Strait, the central portion of the sea and near the southern entrance region [*Simmons et al*., 2004; *Niwa and Hibiya*, 2014], suggesting a rich tidally driven internal wavefield within the Solomon Sea. Winds supply additional energy to the internal wavefield by generating near-inertial waves. The full internal wavefield supplies a potential source of energy for the observed water mass transformations as the breaking of internal waves leads to turbulent mixing. Eddy activity may also influence temporal variability and patterns of mixing [*Whalen et al*., 2012] as the Solomon Sea has an energetic eddy field [*Melet et al*., 2010b; *Hristova and Kessler*, 2012; *Djath et al*., 2014]; however, the eddy-induced temporal variability of mixing remains to be explored.

The New Guinea Coastal Current/New Guinea Coastal Undercurrent (NGCC/NGCU) system of the Solomon Sea is the primary source of the Equatorial Undercurrent (EUC), acting as the direct connection between the South Pacific subtropical gyre and equatorial Indo-Pacific circulation. The physical and biogeochemical water properties that are set by mixing in the Solomon Sea reach the surface when the EUC upwells in the tropical eastern Pacific Ocean [*Tsuchiya et al*., 1989; *Fine et al*., 1994; *Ryan et al*., 2006; *Kashino et al*., 2007; *Grenier et al*., 2011; *Qin et al*., 2016]. The strong shear associated with the NGCC/NGCU is another potential source of energy for turbulent mixing within the Solomon Sea, likely generating shear instabilities along the water mass pathways.

The bulk of our knowledge about the quantitative transformation of water masses in the Solomon Sea is the result of several regional modeling studies [*Melet et al*., 2011; *Djath et al*., 2014]. To model water mass mixing in the Solomon Sea, *Melet et al*. [2011] used a turbulent closure model and additionally the tide-based vertical diffusivity parameterization proposed by *Koch-Larrouy et al*. [2007] for the Indonesian Seas, a group of marginal seas with a topographically contained internal wavefield akin to the Solomon Sea. The parameterization of *Koch-Larrouy et al*. [2007] is adapted from that of *St Laurent et al*. [2002] with two important differences. The first difference is the assumption that all the energy added to the internal wavefield by the tides within the marginal sea of interest is dissipated within that sea. The second difference is a shift in the vertical distribution of energy dissipation from maximum near the bottom of the water column to the thermocline with a dependence on stratification. The *St Laurent et al*. [2002] parameterization was developed for abyssal mixing and assumes that the bulk of internal waves will break over rough topography, thus near the bottom, while *Koch-Larrouy et al*. [2007] assumes dissipation to be maximum in the thermocline for marginal seas. The modeled downstream water properties for *Melet et al*. [2011] are in reasonable but not full agreement with regional observed water mass climatologies. Specifically, the modeled

downstream salinity is biased low by 0.1 psu over the 24.5–27.5 σ_θ range compared to the observed properties, such that the erosion of STMW is too strong in the model while the deeper mixing of AAIW is underrepresented. However, there were relatively few in situ observations available for comparison at the time of the study. A recent study by *Melet et al*. [2016] has shown that processes that influence water mass properties such as ocean heat uptake and thermocline thickness are highly sensitive to the vertical distribution of mixing when simulated by climate models.

Understanding the strength, vertical and horizontal structure of mixing and its sources in the Solomon Sea is of importance for quantifying its influence on water mass transformation and impact on equatorial circulation. As of yet, no direct observations of energy dissipation or mixing have been made in the Solomon Sea. Here we use conductivity, temperature, depth (CTD), and Lowered Acoustic Doppler Current Profiler (LADCP) data from two survey cruises and the global Argo network to infer the rate of dissipation of turbulent kinetic energy and diffusivity throughout the Solomon Sea. In section 2 we outline the data sets and methods used for this analysis. The results and a comparison of the different methods and data sets are given in section 3, with a discussion of the results in section 4 and final remarks in section 5.

2. Data and Methods

2.1. Cruise Data

Hydrographic surveys of the Solomon Sea were completed in 4 July to 1 August 2012 (the cruise Pandora on the R/V l'Atalante) and 28 February to 31 March 2014 (the cruise MoorSPICE on the R/V Thomas G. Thompson) (Figure 1a). The objectives of the cruises were to observe the strength and pathways of the currents in the Solomon Sea, characterize the water masses, and deploy and recover nine moorings in three outflow channels of the Solomon Sea. The experiment was designed for the shipboard surveys to sample different phases of the monsoonal wind forcing as the Southeast Asian monsoon modulates physical processes in the Solomon Sea over a range of spatial scales. Strong and persistent southeasterly winds were observed during Pandora, while MoorSPICE occurred during a neutral phase of the monsoon wind cycle when the winds were weak and sporadic. During Pandora 164 CTD casts were taken, all with simultaneous velocity profiles acquired either from shipboard or lowered ADCP. All MoorSPICE casts also acquired simultaneous CTD and LADCP profiles, and 29 of the 82 casts were at repeat locations with Pandora casts for direct comparison. Further details about these cruises and data processing can be found in *Germineaud et al*. [2016].

As we do not have direct observation of turbulence (microstructure observations) or mixing (dye release experiments) we must use indirect methods to tease out the patterns of mixing. The turbulent dissipation rate (ϵ) was estimated from the cruise data sets using two distinct methods.

2.2. The Thorpe-Scale Method

The first method estimates ϵ from a length scale of temperature and density overturns, known as the Thorpe scale (L_T), following the methods of *Thorpe* [1977] and *Dillon* [1982]. This method takes advantage of an empirical relationship between L_T and the Ozmidov scale, L_O=0.8L_T, and the Ozmidov relation, $L_O=\sqrt{\frac{\epsilon}{N^3}}$ where N is the buoyancy frequency, to estimate the expected dissipation rate of an observed overturn. Outside of the overturn regions L_T is zero and thus ϵ by way of the Ozmidov relation is also zero. *Galbraith and Kelley* [1996] provide a thorough description of the method and its caveats.

Our analysis uses both temperature and potential density profiles from shipboard CTD casts at 0.25 and 1 m vertical resolution, respectively. The vertical resolution of each quantity is determined by the sensor's effective temporal resolution due to spectral noise (4 Hz for temperature and 1 Hz for conductivity) and the CTD fall rate (1 m/s). While density is the optimal quantity to observe overturns, the higher vertical resolution of temperature observations provide an opportunity to estimate L_T from overturns with smaller overturn heights (z_{OT}) that cannot be resolved using density observations. As some overturns in temperature may be stable in density, the Turner angle (θ_T) is calculated which quantifies the relative influence of temperature and salinity on the density gradient as degrees of rotation. Regions of cold, freshwater over warm, salty water that are statically stable have $-90^\circ < \theta_T < -45^\circ$ and are ignored when calculating Thorpe scales from temperature profiles in an effort to be conservative. Using the potential density and temperature observations, two profiles of ϵ are generated: the first simply consists of estimates made using overturns

found in profiles of potential density, while the second is a composite made from the first estimate of ϵ and additionally incorporates ϵ from temperature overturns with smaller z_{OT} that cannot be resolved by potential density observations.

2.3. The Finescale Method

The second method of estimating ϵ follows the finescale parameterization described in *Kunze et al*. [2006] and *Polzin et al*. [2014]. The method relies upon several key physical assumptions, primarily that the turbulent dissipation rate in the ocean is driven by the internal wavefield and that energy cascades downscale via wave-wave interactions to turbulent length scales. The parameterization uses observations of LADCP shear and CTD strain to quantify the strength of the internal wavefield and estimates ϵ by comparing the observed wavefield to the theoretical Garrett-Munk (GM) internal wavefield in wave number spectral space.

Two criteria are applied to remove segments of data in which the shear or strain are likely dominated by processes other than internal waves, and so violate the primary assumption of the method. The first criterion (C1) removes density and velocity observations within the mixed layer where surface and mixed layer processes dominate the shear and strain fields. The mixed layer depth is defined as the depth at which density is 0.03 kg m^{-3} greater than the density measured at 10 m [*de Boyer Montégut et al*., 2004]. The second criterion (C2) removes data from within the strong current cores of the NGCC/NGCU system. The parameterization is not suited for use in a strongly sheared boundary current where it is not possible to differentiate between the shear and strain due to the current versus that due to internal waves [*Polzin et al*., 2014]. All shipboard LADCP was used to construct a mean current core, centered around current maximums. The average profile of the current core has a velocity maximum $\sim$35 cm s^{-1} in the top 1000 m. C2 removes all data above sampled current core. C2 also removes data 100 m below the current core because, on average, the current velocity decreases by 50% 100 m below the local maximum within the NGCC/NGCU system. Although it is expected that the finescale method will perform poorly in regions with large mean shear due to currents, nonetheless *Winkel et al*. [2002] find that using the total shear in the finescale parameterization often is a better predictor of ϵ. Estimates of ϵ will be presented in section 3 with and without C2 applied, as the true dissipation likely lies between these two estimates. C1 and C2 were only applied when using the finescale method and not enforced when using the Thorpe-scale method.

The finescale method applied to a sample cast from the Pandora cruise is shown in Figure 3 and serves as a visual outline of the method. Simultaneous profiles of velocity and density (Figure 3a) with typical vertical resolutions of 10 and 1 m, respectively, are broken into 320 m long, half-overlapping segments. For each segment, we estimate isopycnal strain, $\xi_z = \frac{N^2 - N^2_{fit}}{\bar{N}^2}$, and buoyancy frequency normalized shear, $\frac{\mathbf{U_z}}{\bar{N}}$, where N_{fit} is a cubic fit of the buoyancy frequency, $\bar{N}$ is the segment-averaged buoyancy frequency, and $\mathbf{U_z} = (\frac{\partial u}{\partial z} + i\frac{\partial v}{\partial z})$ (Figure 3b). The spectra of $\frac{\mathbf{U_z}}{\bar{N}}$ and ξ_z are calculated in wave number space (k_z) for each segment (Figure 3c) and are corrected for high wave number attenuation due to signal processing and first differencing (Figure 3d, also see Appendix A for full description). The corresponding GM spectrum is calculated for each segment (Figures 3c and 3d, black lines) and all spectra are integrated over appropriate wave number ranges. The appropriate wave number ranges are described in full in Appendix A. The GM spectrum functions as a nondimensional, standard unit that is used to quantify the strength of the observed internal wavefield relative to the theoretical GM spectra.

The parameterization then uses the variance from the observed and GM strain spectra with additional adjustments for latitude, local stratification, and a regional ratio of shear-to-strain variance to estimate ϵ for each segment (Figure 3e). Estimates of ϵ using the Thorpe-scale method are also shown as gray dots in Figure 3e for direct comparison. A more detailed description of the finescale method and the choices made in the analysis can be found in Appendix A.

2.4. Argo Data

This study additionally utilized an Argo data set consisting of 733 profiles from 77 floats with Iridium communications systems from January 2013 to June 2016 that is within the study region of 2°S, 146°E to 12°S, 164°E (Figure 1b). The Argo program is an international effort that maintains over 3000 freely drifting, profiling floats that measure the temperature and salinity of the ocean's upper 2000 m. Turbulent dissipation estimates are obtained from isopycnal strain using temperature, salinity, and pressure measured by Argo floats and the mean observed ratio of shear-to-strain variance from the shipboard data following the

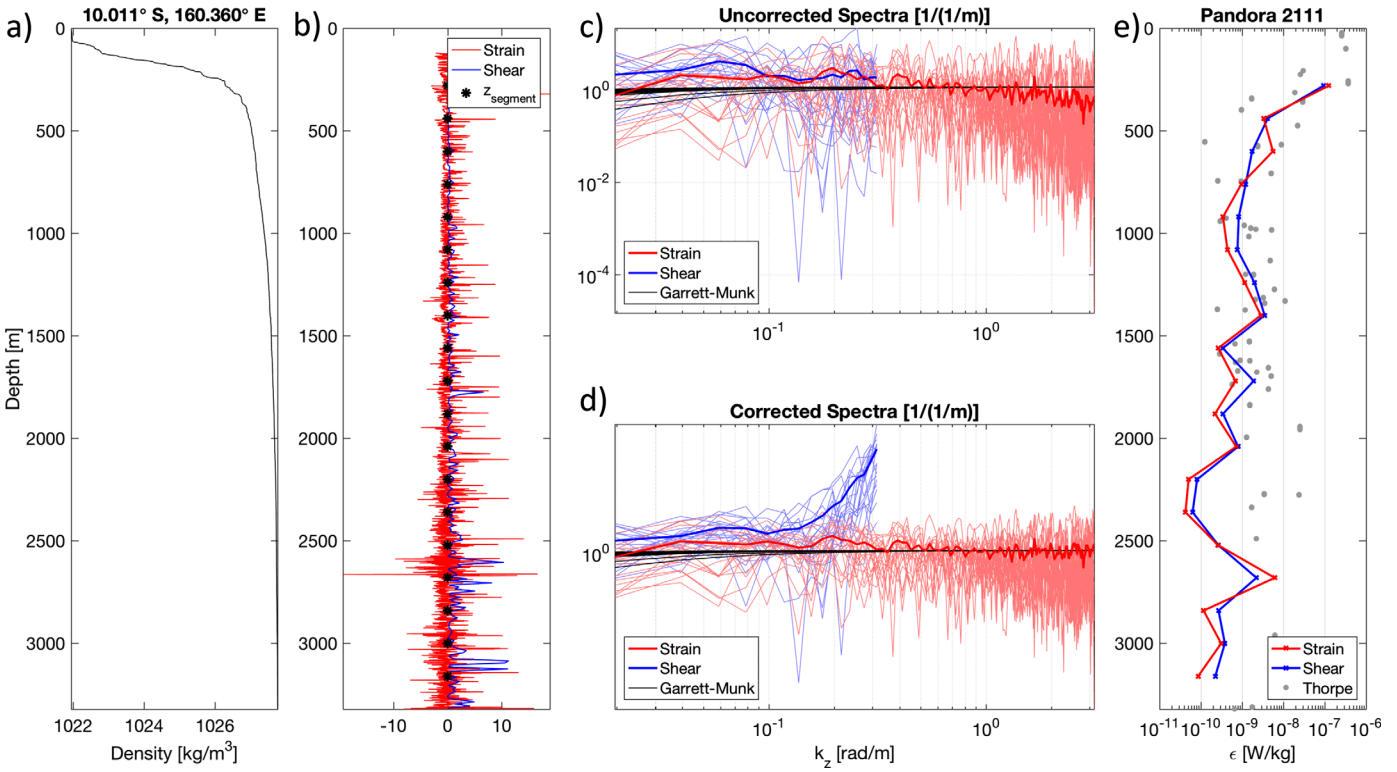

Figure 3. (a) A density [kg m^{-3}] profile at 10.011° S, 160.360° E as a function of depth. (b) The profile of LADCP- and CTD-derived normalized shear (blue line) and CTD-derived strain (red line) during the Pandora cruise (both quantities are unitless). Black stars mark the center point of 320 m segments for which the spectra was used to generate an estimate of dissipation. (c) Uncorrected normalized shear spectra (blue) and strain spectra (red), where the thin lines are from individual segments and the thick lines show the cast mean. The range of GM spectra are in black. (d) Normalized shear spectra (blue) and strain spectra (red) that have been corrected for high wave number attenuation. The line and color scheme is identical to that of Figure 3c. (e) Estimated dissipation [W kg^{-1}] as a function of depth [m] from the Thorpe-scale method (gray) and the finescale shear (blue) and strain (red) parameterization.

methods detailed in *Whalen et al.* [2012]. The Argo profiles of ξ_z were broken into 150 m long, half-overlapping segments with a vertical resolution of 2 m. Shorter segment-lengths (150 m compared to 320 m) were utilized for Argo to maximize the number of ϵ estimates per profile. This efficiency is due to the smaller wave number range required to integrate strain spectra compared to the larger wave number range required for simultaneous shear and strain observations (see Appendix A).

2.5. Comparative Analysis

To facilitate comparison between the different methods and data sets, mean profiles were created by averaging all the estimates of ϵ in 320 m bins from the surface to 2240 m. For the finescale method, mean profiles were generated from dissipation estimates that used strain spectra for more direct comparison with the Argo derived dissipation estimates. The maximum depth of 2240 m was chosen to include all the Argo observations, as the floats typically have a maximum diving depth of 2000 m. Error bars were constructed from the 90% bootstrap confidence level of the mean for each depth bin.

To determine spatial patterns of ϵ, the median finescale dissipation is computed from combined cruise and Argo data sets in 1/2° latitude by 1/2° longitude grid boxes over density ranges corresponding to the thermocline $(STMW, 23.3 < \sigma_\theta < 26.7)$, intermediate $(AAIW, 26.7 < \sigma_\theta < 27.5)$, and deep $(27.5 < \sigma_\theta)$ layers. The isopycnals that delineate each layer approximately correspond to 85, 400, and 1270 m depth in the Solomon Sea. Each grid cell has at least three estimates. Supplementary data sets are utilized to investigate potential sources of spatial variability. Topographic roughness was computed as the variance of bathymetry over 1/2° latitude by 1/2° longitude grid boxes using bathymetry from ETOPO1 1 Arc-Minute Global Relief Model [*Amante and Eakins*, 2009]. This analysis also utilizes the energy input into the baroclinic tide from the barotropic tide from FES2004. FES2004 was produced by LEGOS and CLS Space Oceanography Division and distributed by AVISO, with support from CNES (http://www.aviso.altimetry.fr/).

3. Results

The mean profiles of ϵ for the combined July 2012 Pandora and March 2014 MoorSPICE cruises using the Thorpe-scale method are enhanced in the top 320 m at $1.9-2.3\times10^{-7}$ [W kg^{-1}], decreasing with depth to $2.7-2.9\times10^{-9}$ [W kg^{-1}] at 2000 m (Figure 4a, black lines). While the mean profile of ϵ derived from the composite Thorpe-scale estimates (dotted black line) contains 6.6 times as many overturns as the mean profile from the density Thorpe-scale estimate (solid black line), the resulting slight enhancement of ϵ is not statistically significant. The mean profile of ϵ for the combined cruise data set using the finescale method with C1 and C2 applied is shown in Figure 4a (dotted red line) with a maximum ϵ of 4.1×10^{-8} [W kg^{-1}] in the upper 320 m decreasing to 2.0×10^{-9} [W kg^{-1}] below 2000 m depth. The mean profile of finescale ϵ without C2 applied (Figure 4a, dashed red line) primarily differs from the mean profile of finescale ϵ with C1 and C2 applied above 1000 m depth with a local max of 1.2×10^{-7} [W kg^{-1}]. The mean profile of ϵ from the Argo data set using the finescale method (Figure 4a, solid red line) has a vertical structure that is similar to the shipboard finescale profile below 320 m, but is biased low with a deep minimum of 2.2×10^{-10} [W kg^{-1}] and maximum in the top 320 m of 5.7×10^{-8} [W kg^{-1}]. Depth-mean ϵ from Argo strain within the Solomon Sea is elevated by a factor of 8 compared to ϵ from Argo strain in the Pacific along a similar

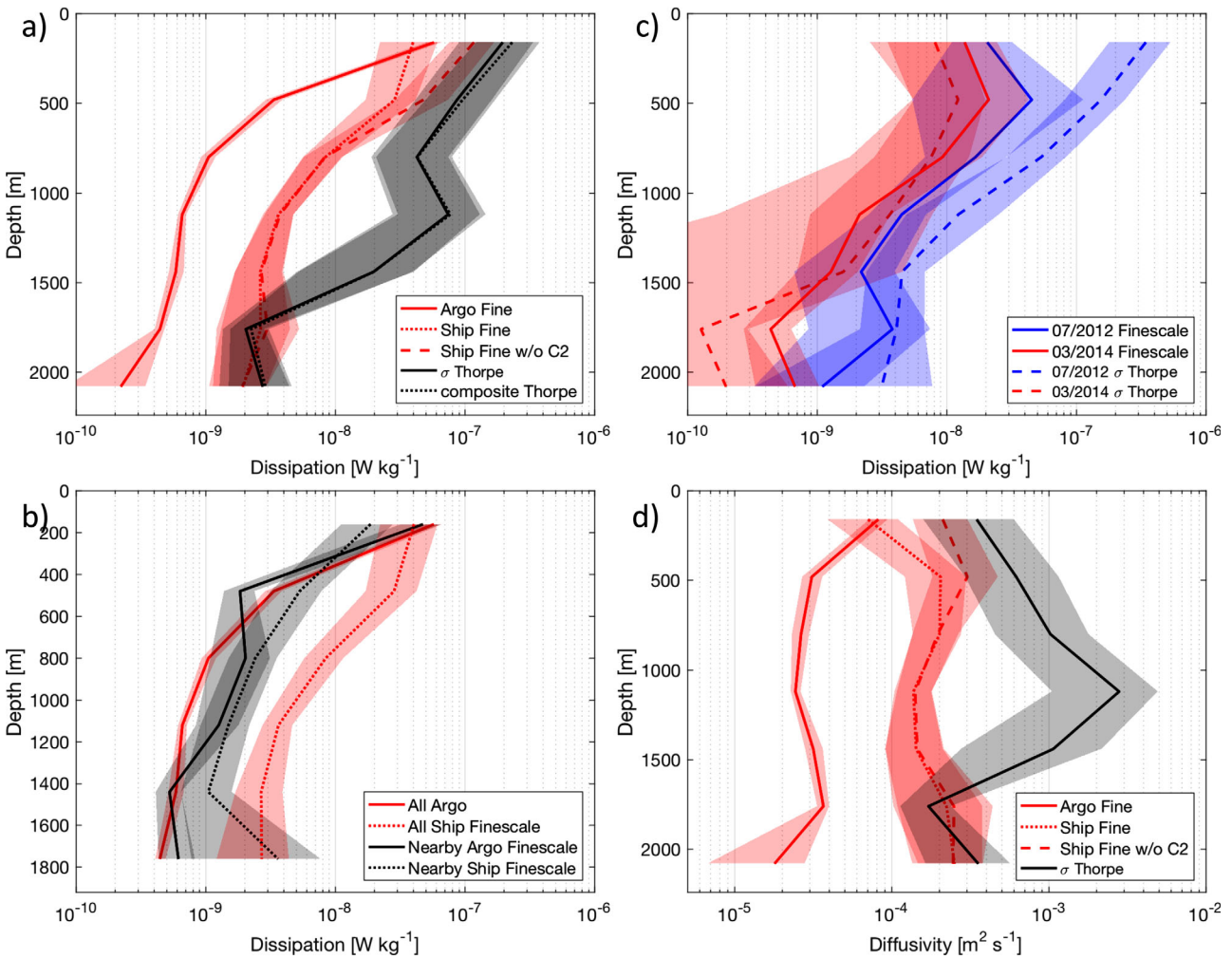

Figure 4. (a) Mean dissipation profiles for Argo strain observations using the finescale method (solid red line) and the combined cruise data using strain observations with the finescale method (dotted and dashed red lines), and density (solid black line) and temperature (dotted black line) observations with the Thorpe-scale method. (b) Mean dissipation profiles from all available Argo (solid red line) and shipboard (dotted red line) finescale observations and from a subset of data using pairs of Argo (solid black line) and shipboard (dotted black line) casts that were within 25 km of each other. (c) Mean profiles of dissipation only from stations repeated during both the Pandora (blue) and MoorSPICE (red) cruises using the finescale parameterization (solid) and the Thorpe-scale method with density (dashed). (d) Profiles of mean diffusivity from the Argo strain observations using the finescale method (solid red line), the combined cruise data using strain observations with the finescale method (dotted and dashed red lines), and the combined cruise density observations with the Thorpe-scale method (solid black line). Shading around all lines give the 90% bootstrap confidence intervals for each mean.

latitudinal band (12°N–12°S) (not shown, *Whalen et al*. [2012]). The mean profile of ϵ in the Solomon Sea from Argo is elevated by a factor 2–10 over the top 2000 m depth compared to that of the equatorial Pacific, though the open-ocean profile has very similar vertical structure with ϵ maximum near the surface and decreasing with depth.

The comparatively weak maximum in the cruise finescale profile compared to the Argo finescale profile is largely due to C2 described in section 2, which reduces the mean ϵ from the cruise finescale estimates in the top 320 m by a factor of 3, but does not significantly affect deeper means. The overall low bias of the Argo mean profile compared to the cruise data is due largely to sampling patterns of the two data sets; cruise data are concentrated around regions of rough topography within the NGCC/NGCU system (Figure 1a) while Argo data are more evenly dispersed throughout the region (Figure 1b). The bias due to spatial sampling accounts for 83% of the RMS difference between the mean profiles of ϵ below 320 m. The bias was determined using a subset of the data that only contains pairs of Argo and cruise casts within 25 km of each other (Figure 4b). The remaining fraction of the RMS difference is likely due to temporal variability of the sampling and dynamical processes.

The local maximum found near 1200 m in Thorpe scale ϵ (Figure 4a, black lines) is the largest discrepancy in profile structure between the Thorpe and finescale methods. This local maximum is the result of two stations where repeated casts resolved the presence and evolution of two relatively large overturns, with large z_{OT} ($\sim$150 m), weak N ($\approx$ 0.002 rad/s), and large L_T ($\approx$ 15 m) (Figures 5a and 5e). Both stations lie on the edges of the basin and within the strongly sheared boundary currents (Figure 1a, cyan and magenta stars). While the outer scales of the overturns at each stations are quite similar, the vertical structure of the density at each station is visually distinct, suggesting that different mechanisms may be responsible. A potential mechanism could be shear instability due to the NGCC/NGCU system. To investigate, density and velocity are smoothed and subsampled to 20 m vertical resolution and used to calculated N^2, shear squared (S^2) and inverse Richardson number $(Ri^{-1} = \frac{S^2}{N^2})$. When $Ri^{-1} \geq 4$ the shear is sufficient to overturn stratification and is suggestive of shear instability. A critical Ri^{-1} is necessary for the generation of shear instabilities but alone is not a sufficient condition. Stratification is quite similar between the two stations with the overturn region in MoorSPICE having slightly lower values of N^2 compared to Pandora, though the overturns occur at different depths (Figures 5b and 5f). However S^2 is an order of magnitude larger at the MoorSPICE overturn compared to the Pandora station (Figures 5c and 5g), resulting in more instances where $Ri^{-1} \geq 4$ (Figures 5d and 5h). These results predict, but do not guarantee, that shear instabilities are driving the observed density overturns at the MoorSPICE station. The shear field present in the Pandora observations is insufficient at this scale to generate shear instabilities, though it may be sufficient at smaller, unresolved scales. The Pandora density overturns may be driven by a different mechanism.

The dissipation associated with these large overturns was 2–3 orders of magnitude larger than the dissipation estimated by the finescale method over the same depth ranges. These overturns thus skew the Thorpe mean dissipation for all shipboard data between 1000 and 1500 m depth. Removal of the casts in question from both the finescale and Thorpe mean profiles reduces the mean difference between the profiles by $\sim$30% and the subsurface maximum in the mean Thorpe profile disappears (not shown). *Mater et al*. [2015] found that L_T/L_O increases with increasing overturn size leading to overestimates of ϵ by the Thorpe-scale method; however, when profiles of ϵ from Thorpe and microstructure observations are depth-averaged over time, Thorpe ϵ is biased high but within an order of magnitude compared to microstructure ϵ. Thus, large and strong overturns may bias estimates of ϵ high when using the Thorpe method; nonetheless, these overturns are contributing to the dissipation of energy in a way that the finescale method is not able to capture.

Temporally variable dynamics of the Solomon Sea, such as monsoonal winds, likely vary ϵ seasonally by generating near-inertial waves and modulating upper ocean dynamics. To explore this seasonal variability, the mean profiles of ϵ for each method and cruise are compared using the profiles from repeated stations (Figure 4c). Limiting the data to only repeated locations should reduce the differences between the mean profiles that could be attributed to spatial variability, potentially highlighting the temporal variability of ϵ. The finescale depth-average of ϵ for the top 2000 m is elevated by a factor of 2.3 during the July 2012 cruise relative to the March 2014 cruise (Figure 4c, solid lines). The mean finescale profile for July is higher at all depths compared to March. Mean dissipation profiles from Argo observations averaged over the same

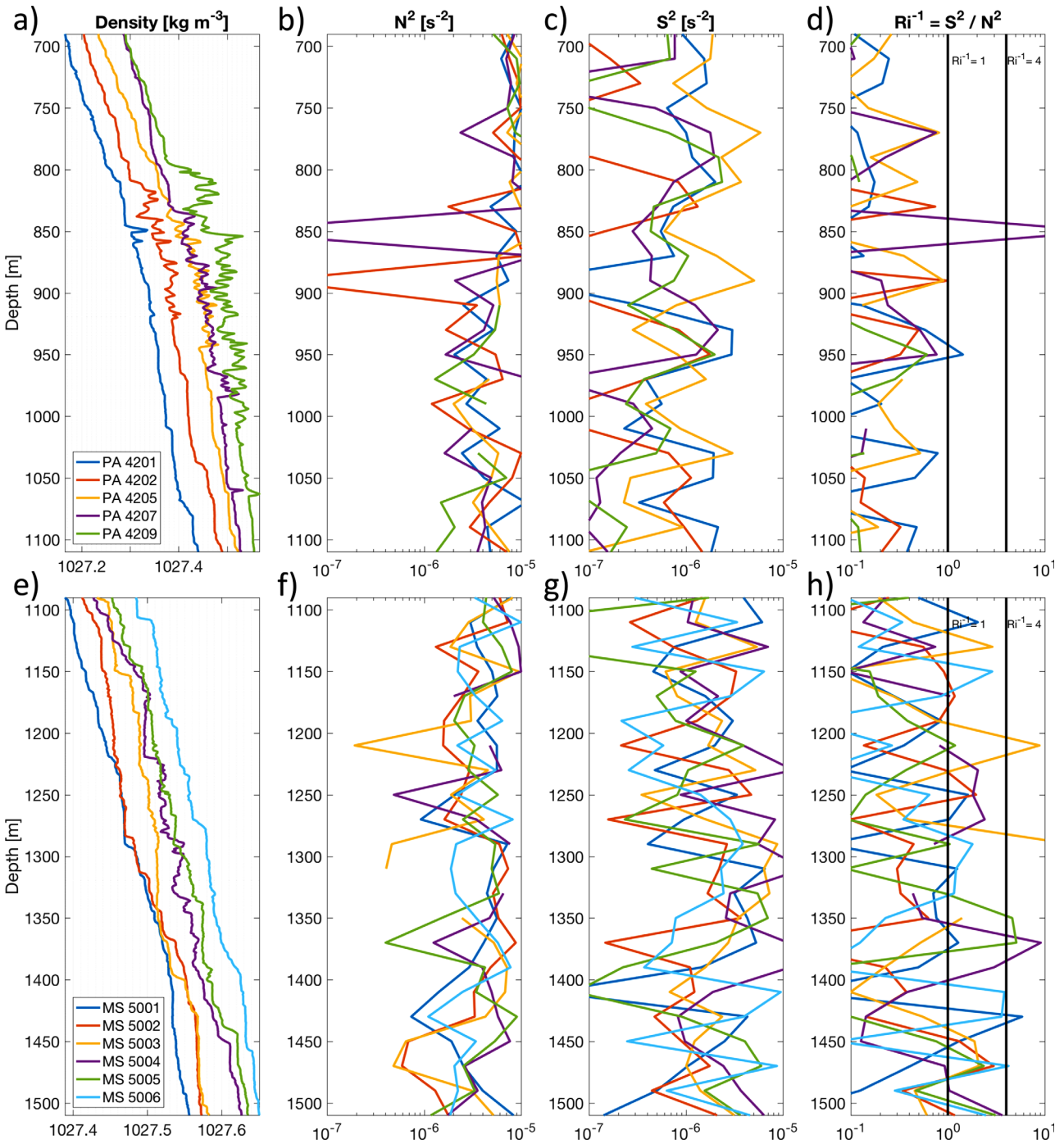

Figure 5. (a, e) Density, (b, f) N^2, (c, g) shear squared (S^2), and (d, h) inverse Richardson number (Ri^{-1}) for the repeat casts from (a-d) Pandora station 42 (5.1°S, 153.3°E) and (e–h) MoorSPICE station 50 (11.5° S, 154.6° E). There is an (a) 0.03 and (e) 0.01 kg m^{-3} offset between successive density profiles for clearer visualization of the developing overturns.

months find a consistent though weaker relationship with mean July dissipation a factor of 1.5 larger than in March (not shown). Depth-averaged ϵ from density overturns using the Thorpe method also show July 2012 dissipation rates are elevated relative to March 2014 but with depth-averaged ϵ 16.0 times larger in July 2012 (Figure 4c, dashed lines). The mean Thorpe profile for July is higher above 1000 m and below 1500 m relative to the March observations. The composite Thorpe-scale estimate for March 2014 is significantly larger in the top 320 m compared to the density estimate (not shown) and depth-averaged ϵ is 13.1 times larger in July 2012.

As the barotropic tide passes over rough topography, internal tides are generated and break, enhancing dissipation and providing another source of temporal variability at higher frequencies than seasonal variability. Fortnightly modulation of mixing near-rough or abrupt topography due to the spring-neap cycle of the barotropic tide has been well resolved in process studies [*St. Laurent et al.*, 2001; *Klymak et al.*, 2006; *Levine and Boyd*, 2006; *Klymak et al.*, 2008]. These process studies suggest that the fortnightly modulation of ϵ is confined in space to near-generation sites, with ϵ relaxing to background levels hundreds of meters above the bottom and tens of kilometers away. The relationship between finescale ϵ from observations within 500 m of the bottom and the strength of the barotropic tide predicted by the TPXO model [*Egbert and Erofeeva*, 2002] is investigated. A positive but statistically insignificant relationship $(R^2=0.1)$ is found between these quantities. While ϵ near-rough topography is likely modulated at tidal frequencies, only one third of the finescale profiles are full depth with the majority of those observations over relatively smooth topography making such a signal difficult to detect.

Now we will focus on the two-dimensional patterns of ϵ over three isopycnal layers and within 500 m of the bottom. Spatially the clearest pattern is the decreasing magnitude of finescale ϵ with increasing density and thus depth (Figure 6). In the thermocline layer (Figure 6a), the strongest dissipation is concentrated at the edges of the Solomon Sea with the weakest dissipation south of New Britain in the interior. At intermediate isopycnals (Figure 6b), dissipation is enhanced around Vitiaz and Solomon Straits and on the western margin where topography is highly variable. Away from the margins, a north/south asymmetry in the magnitude and spatial variability of dissipation is visible in both the intermediate and deep isopycnal ranges (Figures 6b and 6c), likely related to the north/south asymmetry in topographic roughness. For these layers there is also a marked difference in the spatial variability of dissipation within the Solomon Sea, compared to the relative homogeneity of the dissipation in the equatorial band of observations outside of the Solomon Sea from 2°S, 155°E to 4°S, 164°E. Due to the deep nature of the Solomon Sea (bottom depths

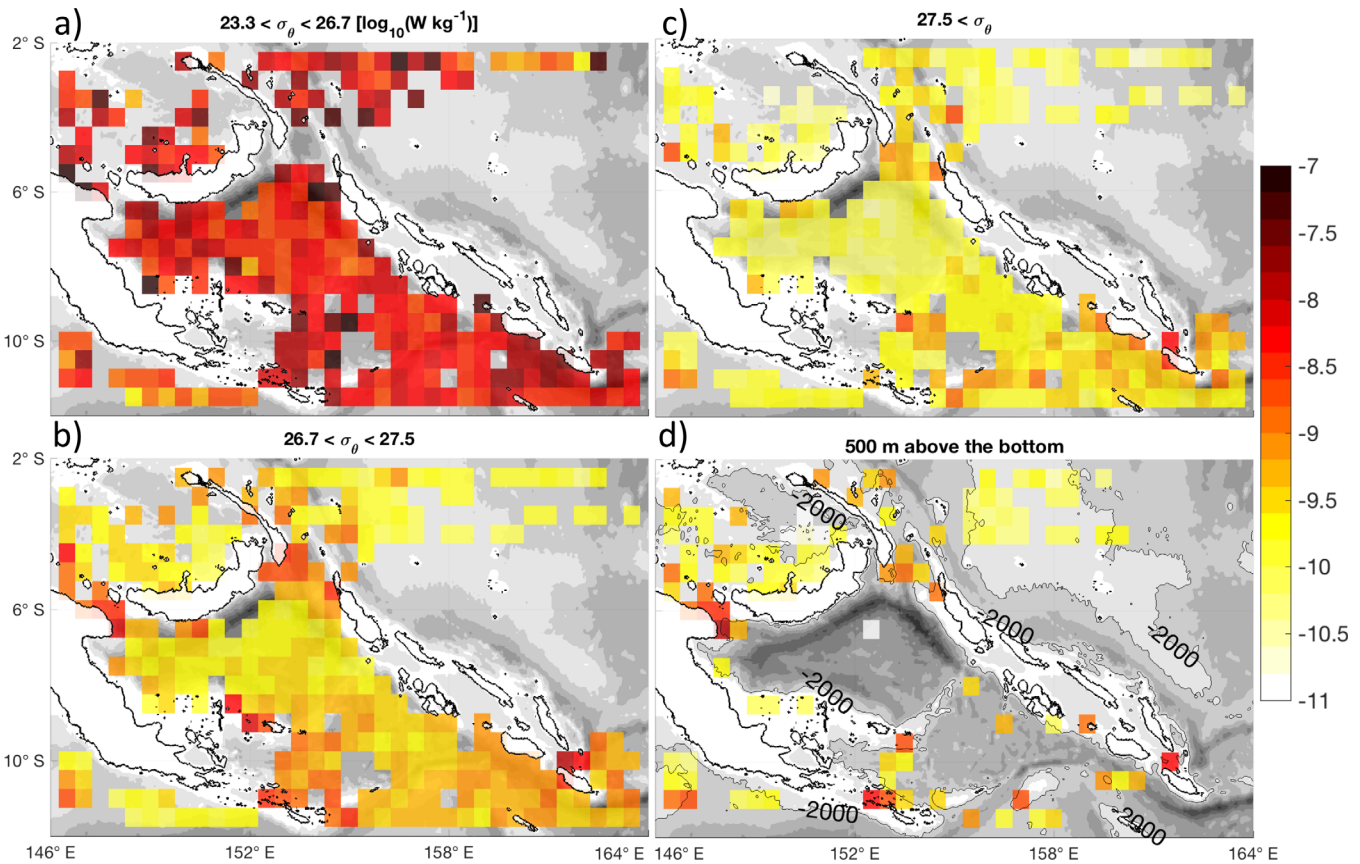

Figure 6. The log of median dissipation [W kg^{-1}] from combined cruise and Argo data sets using the finescale method in (a) the thermocline which contains STMW $(23.3 < \sigma_\theta < 26.7)$, (b) the intermediate layer which contains AAIW $(26.7 < \sigma_\theta < 27.5)$, (c) the deep layer $(27.5 < \sigma_\theta)$, and (d) within 500 m above the bottom at $\frac{1}{2}^\circ \times \frac{1}{2}^\circ$ resolution. Bathymetry is contoured at 1000 m intervals and the coast is drawn in black. The 2000 m isobath is also contoured and labeled in black for Figure 6d.

>2000 m in >50% of the sea), only one third of the total observations extend to the bottom and so can be utilized to investigate near-bottom patterns of ϵ (Figure 6d). In those profiles that do extend to the bottom, enhanced dissipation is observed over regions of abrupt or rough topography while lower ϵ is associated with smooth and flat topography.

4. Discussion

The Solomon Sea is a marginal sea where energetic currents and tides encounter abrupt and rough topography. Observations from two field campaigns and the Argo database were used to estimate ϵ throughout the region via the Thorpe-scale method and finescale parameterization. The mean profile of ϵ in the Solomon Sea is maximum near the surface ($4.1-23\times10^{-8}$ [W kg^{-1}]) and decreases with depth ($2.2-29\times10^{-10}$ [W kg^{-1}]) (Figure 4a). Depth-mean ϵ in the Solomon Sea is elevated by a factor of eight relative to the rest of the equatorial Pacific using Argo strain observations. Spatial patterns of ϵ vary up to 2 orders of magnitude over isopycnal layers that contain the STMW and AAIW within the Solomon Sea (Figure 6). Shipboard and Argo data sets suggest seasonal variability of ϵ with elevated dissipation coincident with strong monsoonal winds (Figure 4c), though the full seasonal cycle of dissipation remains unresolved by this data set.

4.1. Thorpe Versus Finescale Method

Because the Thorpe and finescale methods estimate ϵ using different assumptions, it is not entirely surprising that when the methods are applied to the same data set the results differ slightly. The Thorpe-scale method relies entirely on the presence of density overturns within a water column, regardless of the source of the instability. Thus, the estimate can quantify ϵ resulting from a suite of physical processes, including but not limited to breaking internal waves. The finescale method, on the other hand, assumes the observed shear and strain over vertical length scales of internal waves is solely due to internal waves and that the wavefield will drive a particular rate of dissipation. Thus any shear and strain from other physical processes with similar vertical length scales may bias the estimated ϵ using the finescale method to higher values. While great care is taken to reduce this bias, particularly in the upper ocean where contamination from mesoscale and smaller scales is greatest, there is likely some residual contamination that is difficult to avoid. Even when well executed, the method only attempts to predict dissipation due to the energy in the internal wavefield, which is not the only energy source supplying dissipation and mixing (shear instabilities within the boundary currents present one additional source).

Thus, we might expect the methods to agree best in regions where internal waves are the dominant process supplying energy for dissipation, such as in the deep ocean. Indeed, the estimates of mean ϵ from the cruise data converge below 1500 m and fall within the 90% boot-strap confidence intervals (Figure 4a). Over the entire water column, Thorpe-scale estimates of ϵ are on average a factor of 3 larger than finescale strain estimates. Similarly in the Drake Passage *Thompson et al*. [2007] found Thorpe-scale estimates were consistently elevated by a factor of $2-3$ compared to finescale estimates from the same data set. These results indicate that the Solomon Sea internal wavefield is an important source of energy for dissipation and mixing. However in the top 1500 m when Thorpe estimates exceed finescale estimates by more than a factor of 3, other processes may also contribute to energy dissipation.

4.2. Method Uncertainties

While the shipboard observations using the Thorpe and finescale methods suggest elevated dissipation in the surface and thermocline with weaker dissipation in the deeper layers, there remains uncertainty in the magnitude of these estimates relative to the "true" ϵ. The most accurate observations of ϵ come from shear microstructure profilers, which resolve shear at dissipative length scales, enabling direct estimates of ϵ assuming isotropic turbulence [*Oakey*, 1982]. Two regional studies in the Southern Ocean [*Frants et al*., 2013; *Waterman et al*., 2014] use simultaneous observations of microstructure shear and CTD density to compare microstructure derived ϵ with Thorpe and finescale estimates and so offer guidance as to expected differences.

Frants et al. [2013] compared different estimates of ϵ made in two energetically different locations: a smooth abyssal plain in the Southeastern Pacific and the highly energetic Drake Passage. Agreement between Thorpe and microstructure dissipation was best in the strongly dissipative Drake Passage, where Thorpe estimates were generally biased high but differed from microstructure by less than an order of magnitude.

In the quiescent Southeastern Pacific, Thorpe estimates were consistently biased high by at least 1 order of magnitude in the top 600 m with a smaller but still statistically significant bias below. The low stratification of the Southern Ocean decreases the signal-to-noise ratio when quantifying overturns and contributes to the high bias of the Thorpe-scale ϵ. Finescale and microstructure estimates generally agreed within a factor of 2–3 for both locations and captured regional patterns found in the microstructure observations better than Thorpe-scale estimates.

Waterman et al. [2014] found that at depths of 1500 m above the bottom the ratio of shear microstructure ϵ to finescale strain ϵ fell within the factor of two uncertainty predicted for the finescale method by *Gregg* [1989] and *Polzin et al*. [1995]. For a subset of locations, the finescale method systematically overpredicted ϵ within 1500 m of the seafloor. These locations were characterized by high Froude numbers, strong near-bottom velocities and elevated topographic roughness, suggesting the generation and presence of lee waves. It is not surprising then that the finescale parameterization failed to accurately predict ϵ at these locations given that the shear and strain fields are likely dominated by lee waves and wave-mean flow interactions as opposed to freely propagating internal waves for which the finescale parameterization is designed.

These studies suggest that the Thorpe method, particularly in regions of low stratification, gives high-biased estimates of ϵ. In regions of strong stratification, like the Solomon Sea, where the signal-to-noise ratio of density observations is large, accuracy of the Thorpe-scale ϵ and agreement between Thorpe-scale and microstructure ϵ are expected to improve. *Koch-Larrouy et al*. [2015] find good agreement between the Thorpe and microstructure methods in the Indonesian Seas using station-averaged profiles, where stratification is also strong. Finescale estimates qualitatively match regional patterns of microstructure derived ϵ and quantitatively agree within a factor of 2–3, except in regions where processes aside from internal waves contribute significantly to the observed shear and strain fields. The "true" mean profile of dissipation from the cruise data likely lies somewhere in between the finescale and Thorpe method estimates, with maximum ϵ near the surface $O(10^{-7})$ [W kg^{-1}] and decreasing in magnitude to $O(10^{-9})$ [W kg^{-1}] by 2000 m depth.

Whalen et al. [2015] compares finescale strain estimates of ϵ using Argo profiles with microstructure observations at six dynamically diverse locations. In this study microstructure and Argo finescale observations were not taken simultaneously, but rather with measurements separated over a range of timescales. For 96% of the observations, mean microstructure and finescale estimates differ by a factor of 2–3, consistent with the findings of *Frants et al*. [2013] and *Waterman et al*. [2014]. Thus, we expect the regional patterns shown in Figure 6 to be representative of internal wave-driven dissipation variability in the Solomon Sea. Furthermore we would expect mean microstructure observations to match mean finescale estimates within a factor of 3 for all Solomon Sea measurements outside of the NGCC/NGCU system.

4.3. Diffusivity

While the rate of dissipation of kinetic energy is an important quantity, particularly when investigating ocean energy budgets, a related and equally important quantity is diapycnal eddy diffusivity (κ). Practically, κ is estimated using the Osborn relation [*Osborn*, 1980], $\kappa=\gamma\frac{\epsilon}{N^2}$, which assumes that the dissipation of kinetic energy by turbulence results in diapycnal mixing with an empirically determined mixing efficiency (γ) of 0.2. The value of γ has been shown to vary over the life cycle of instabilities and the resulting turbulence. However, 0.2 represents the overall efficiency well and is suitable for use in averaged observations where it is not possible to determine at what stage in the turbulence life cycle observations were made [*Peltier and Caulfield*, 2003]. The resulting mean profiles of κ, using N^2 averaged over the same depth ranges as mean ϵ, are given in Figure 4d. Bin-averaged N^2 for shipboard and Argo observations within the Solomon Sea are maximum at the surface and decrease by 2 orders of magnitude by 2000 m depth with a vertical structure similar to Argo ϵ (not shown). Because the vertical profile of Argo ϵ spans 3 orders of magnitude compared to the 2 orders that its mean profile of N^2 spans, Argo κ retains the vertical structure of enhanced mixing at the surface. The smaller span of magnitude for shipboard ϵ leads to local minima in κ near the surface and more uniform vertical structure with depth for finescale κ without C2. The local maximum for density Thorpe-scale ϵ at 1200 m (Figure 4a, red line) becomes a pronounced subsurface maximum for κ due to the relatively weak stratification at that depth (Figure 4d, red line). The

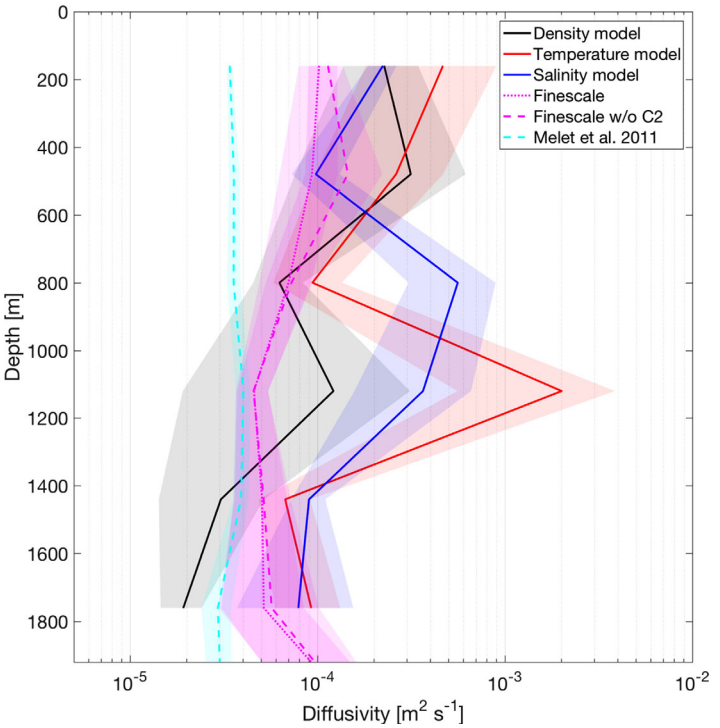

Figure 7. Profiles of bin-averaged κ [m^2 s^{-1}] from the diffusive model using density (black line), temperature (red line), and salinity (blue line) as the tracer. The dotted magenta line shows the profile of bin-averaged observed diffusivity from ship and Argo observations within the water mass pathway between the southern entrance and Vitiaz Strait and the dashed magenta is the same without C2 applied. The dashed cyan line shows the profile for the tide-based parameterization of κ from *Melet et al.* [2011] sampled at the same locations as the finescale observations. The locations of the Argo and shipboard observations used to determine along-path mean κ are shown as magenta dots in Figure 1b. Shading around all profiles give the 90% bootstrap confidence intervals for each mean.

large variation of N^2 in the vertical makes the vertical structure of κ particularly sensitive to ϵ in the Solomon Sea.

In an effort to build confidence in the estimated magnitude of ϵ and thus κ, a simple model that approximates the diffusion of tracers is employed to achieve an independent estimate of κ for comparison with observational-based estimates. The diffusive model, $\frac{\partial}{\partial t} = \kappa \frac{\partial^2}{\partial z^2}$, is applied to the tracers temperature, salinity and density. This model ignores the complexity of the system, such as surface heat and buoyancy fluxes, and main purpose is for comparison with the magnitude and depth structure from the observed profiles of κ. Mean profiles of each tracer (10–2000 m depth, 2 m vertical resolution) are estimated from Argo profiles in the Solomon Sea water mass inflow region (13°S–11°S, 153°E–156°E) and outflow region north of Vitiaz Strait (7°S–4°S, 146°E–148°E) (Figure 2). *Melet et al.* [2011] find that the majority of transport through Vitiaz Strait originates from this narrow inflow region at the southern entrance to the Solomon Sea. The modeled water mass transit times between the two locations from *Melet et al.* [2011, Table 3] are used for the temporal derivative. Profiles of κ that are bin-averaged in depth and their corresponding 90% bootstrap confidence intervals from the diffusive model are shown in Figure 7. In addition, a mean profile of κ derived from all finescale observations along the water mass pathway between the southern entrance and Vitiaz Strait is shown in Figure 7 with the locations of the corresponding observations marked by magenta dots in Figure 1b.

The profiles from the diffusive model are generally maximum near the surface at $2.2-4.7\times10^{-4}$ [m^2 s^{-1}] and decrease with depth to $1.9-9.2\times10^{-5}$ [m^2 s^{-1}]. Depth-means of κ from density give the lowest estimate below 600 m while the error bars of κ from density encompass the estimates from temperature and salinity above 600 m. Thus, using density as our tracer gives a lower bound to the estimate of κ. Below 600 m depth, mean salinity and temperature-derived κ exceed density-derived κ. This suggests that isopycnal stirring, in addition to diapycnal mixing, may significantly contribute to water mass modification. *Melet et al.* [2011] finds that while $\approx 69-83\%$ of the observed water mass modification is diapycnal along this pathway for surface and thermocline waters, diapycnal mixing only accounts for 39% of modification along the intermediate isopycnals.

The mean κ from all finescale strain observations (ship and Argo) within the Vitiaz Strait water mass pathway has a similar magnitude compared to that predicted by the diffusive model but is nearly uniform with depth (Figure 7, dotted magenta line). Again when C2 is not applied there is a relative increase in the finescale mean profile above 1000 m depth (Figure 7, dashed magenta line). The tide-based parameterization of κ from the simulation by *Melet et al.* [2011] sampled at the locations of the finescale observations has a similar order of magnitude as κ from both the observations and the simple model, particularly below 1000 m

depth (Figure 7, dashed cyan line). This mean profile only attempts to predict mixing resulting from internal tides and does not include mixing from the turbulent closure model also used in the original simulation. The parameterization additionally has an upper bound of 10^{-4} [m^2 s^{-1}] potentially biasing the modeled κ low. Nonetheless, it is encouraging that the different estimates of κ have similar magnitudes at depth where internal waves likely dominate mixing.

4.4. Spatial Patterns

The vertical structure of the mean Argo dissipation in the Solomon Sea is very similar to the mean profile of dissipation in the Indo-Pacific over the same latitudinal range, but depth-averages are factor of 2–10 larger in the Solomon Sea (not shown) [*Whalen et al.*, 2012]. We might expect a relatively large dissipation rate in the Solomon Sea compared to the rest of the equatorial Indo-Pacific due to differences in topography. The Solomon Sea has several topographic features that have been identified as sources of internal waves: Solomon Strait and the two undersea ridges in the Southern half of the basin (Figure 1a) [*Simmons et al.*, 2004]. Additionally since the Solomon Sea is partially enclosed, internal waves may reflect off the steep walls of the basin, trapping the internal wave energy in the basin and creating a rich field of shear and strain compared to open-ocean conditions.

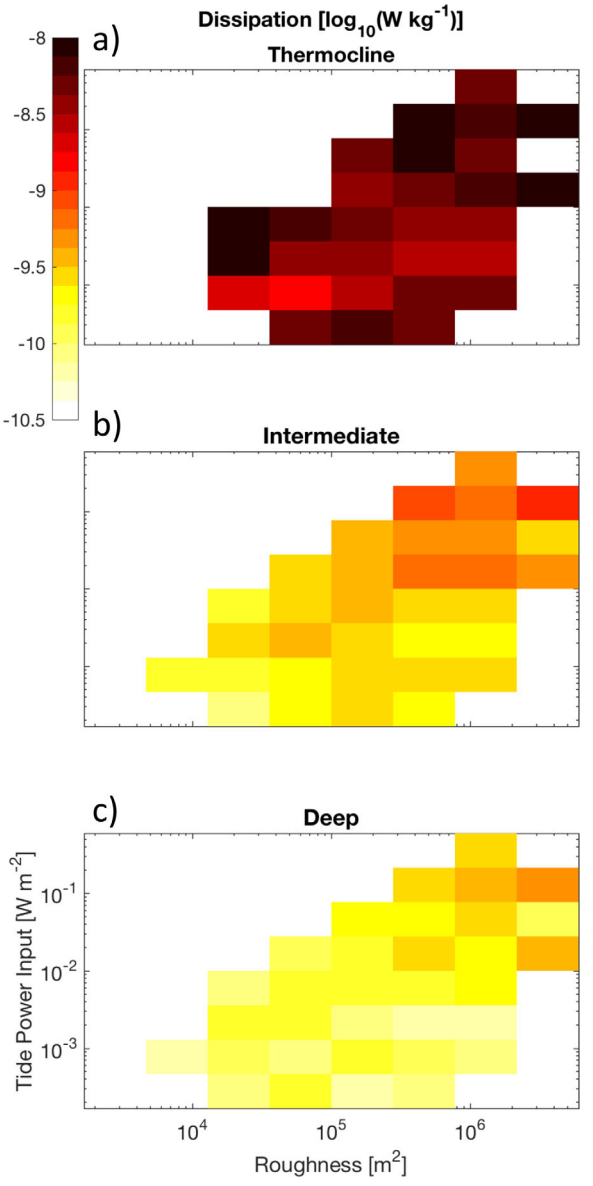

Figure 8. The log of median dissipation [W kg^{-1}] over the (a) thermocline ($23.3 < \sigma_\theta < 26.7$), (b) intermediate ($26.7 < \sigma_\theta < 27.5$), and (c) deep ($27.5 < \sigma_\theta$) density layers as a function of topographic roughness [m^2] and tide power input [W m^{-2}]. The color bar limits are the same for all panels.

In the three isopycnal layers investigated here, ϵ spans at least 2 orders of magnitude making ϵ within the Solomon Sea highly variable along water mass pathways (Figure 6). Thus, the pathway and residence time of water masses traveling through the Solomon Sea will determine how much water masses are modified. The patterns of dissipation along the intermediate (AAIW) and deep isopycnal layers are well correlated with tide power input and topographic roughness (Figures 8b and 8c), suggesting tidally generated and locally dissipated internal waves are of first-order importance for the spatial patterns of mixing along those isopycnals. Patterns of near-bottom ϵ (Figure 6d) are consistent with mixing resulting from the tides and rough topography, though coverage is relatively sparse due to the deep bottom depths of the Solomon Sea. Dissipation in the thermocline (STMW) layer does not display such an obvious correlation to either tidal power input or topographic roughness which may be expected if mixing is not dominated by internal tides (Figure 8a), though internal waves generated by the barotropic tide are likely still important for mixing in the thermocline. Other processes that generate internal waves and drive mixing that are temporally and spatially variable likely construe these patterns in a mean sense. The mean fields of dissipation for all three isopycnal layers have no clear relationship with wind power input or eddy kinetic energy (not shown). Both wind power input and

eddy kinetic energy have large seasonal variability in the Solomon Sea with spatial patterns that change dramatically over the seasonal cycle. Wind power input and eddy kinetic energy likely modulate the strength of mixing in the upper ocean but their effect on ϵ and the potential phase lag between ϵ and these processes requires a well resolved seasonal cycle of the patterns of ϵ in the Solomon Sea.

4.5. Seasonal Changes

Mean Thorpe-scale ϵ from duplicate shipboard stations suggest seasonal variability of dissipation with ϵ enhanced in July and decreased in March (Figure 4c, dashed lines). Shipboard and Argo finescale additionally find ϵ to be enhanced in July compared to March, though to a lesser degree. Temporal changes in ϵ are generally related to variability in internal wave generation [*Alford*, 2003a] and/or changes in large-scale eddy kinetic energy, current shear, and stratification that can influence and interact with internal wave-driven turbulence [*Whalen et al*., 2012; *Moum et al*., 2013].

Near-inertial waves are generated when atmospheric winds input energy into the surface mixed layer causing oscillations at the base of the mixed layer at the local inertial frequency which propagate equatorward and are an important part of the internal wavefield. Temporal variability in wind power input is thus responsible for changes in near-inertial wave generation [*Alford and Whitmont*, 2007]. The Solomon Sea monsoonal wind forcing is characterized by strong wind stress in July and weak wind stress in January and may drive a corresponding seasonal cycle in near-inertial waves and associated turbulent mixing. A preliminary estimate of the mean annual cycle of power input into the near-inertial wavefield integrated over the study region is computed using the method and data described in *Alford* [2001, 2003b] and *Simmons and Alford* [2012]. Using that data, power input in the present study region is enhanced in July compared to March by a factor of 1.8. The seasonal cycle of wind power input for the region is maximum in July to September and minimum in January to March, consistent with the local monsoonal wind forcing which dominates the seasonal variability of wind stress for the Solomon Sea [*Tomczak and Godfrey*, 2013]. A more comprehensive analysis of the seasonal cycle of internal wave energy from mooring data in this study region is now underway.

The monsoonal winds also drive a seasonal cycle in the wind stress curl that results in a seasonally variable eddy kinetic energy field at a 3 month lag [*Hristova and Kessler*, 2012; *Gourdeau et al*., 2014; *Hristova et al*., 2014; *Djath et al*., 2014]. *Whalen et al*. [2012] find that temporal and spatial variations in ϵ are positively correlated with eddy kinetic energy which they hypothesize has to do with internal wave-eddy interactions that enhance turbulence. Thus, we might expect the Solomon Sea eddy kinetic energy to modulate ϵ seasonally as well. In addition, satellite, mooring, and shipboard observations find that the NGCC/NGCU system has seasonal variability in strength, direction, and structure [*Murray et al*., 1995; *Melet et al*., 2010b; *Germineaud et al*., 2016], thus changing the large-scale horizontal and vertical shear fields. This may result in seasonal variability of shear instabilities and/or wave-current interactions [*Moum et al*., 2013]. A final temporally variable mechanism that may be of interest is lee wave generation by the NGCC/NGCU system. The currents' shifting pathways, depth, and strength will result in the NGCC/NGCU system interacting with shallow and rough topography, particularly in Vitiaz Strait where strong near-bottom velocities have been observed [*Murray et al*., 1995], influencing lee wave generation and strength.

5. Final Remarks

Correctly representing the vertical structure, spatial patterns and temporal variability of mixing in the Solomon Sea is key for accurately modeling water mass modification and regional climate [*Melet et al*., 2016]. *Koch-Larrouy et al*. [2010] and *Kida and Wijffels* [2012] demonstrate that accurately representing tidally driven mixing is important for modeled sea surface temperature, rain and wind in the marginal Indonesian Seas that then directly affect tropical climate via ocean-atmosphere interactions. In the Solomon Sea it appears that tides and topographic roughness are, as expected, appropriate quantities to base a parameterization of mixing upon for deep and intermediate layers. In the thermocline however such quantities are likely insufficient. Temporally and spatially variable parameterizations are likely required to accurately predict thermocline water transformation. Mooring observations and long-term Argo observation may help clarify the seasonal cycle and phasing of thermocline mixing relative to local atmospheric forcing, which is the subject of ongoing work. Comparing the total parameterized κ from turbulent closure models and internal tide estimates with observed κ remains an open question for understanding and correctly parameterizing upper ocean mixing in the Solomon Sea.

While great strides have been made to understand transport pathways and low-frequency variability of mesoscale processes in the Solomon Sea, the region likely contains a host of unresolved small-scale processes (beyond freely propagating internal waves) that influence mixing. Vitiaz Strait and St. Georges Channel are both narrow channels with sills at ~1000 m depth and strong velocities (>1 m s^{-1}) at the core. With the addition of the barotropic tide, these straits potentially generate hydraulic jumps and/or lee waves, both of which can result in deep turbulent mixing. Numerical and/or observational process studies could investigate the presence and strength of these processes in the Solomon Sea. Mixing in these straits could be important because it occurs within the largest water mass pathways with direct connections to the EUC and the equatorial Indo-Pacific.

Since dissipation varies by up to 2 orders of magnitude within isopycnal layers, it remains unclear whether strong mixing with short residence times or weaker mixing with longer residence times are more important for water mass modification in the Solomon Sea. Regions of intense mixing (channels, along the southwest boundary, see Figure 6) are colocated with strong current velocities implying that while the water masses transported along those pathways undergo vigorous mixing compared to slower pathways in the interior, the water mass is exposed to these turbulent processes for a relatively brief amount of time. Quantifying the relative influence on water mass modification of these different cases (weak mixing with long residence times vs. strong mixing with short residence times) remains an important question for understanding and accurately modeling ocean circulation.

Appendix A: Finescale Parameterization

The finescale parameterization is based on two physical quantities, isopycnal strain, ξ_z, and buoyancy frequency normalized shear, $\frac{\mathbf{U}_z}{\hat{N}}$, where $\mathbf{U}_z = (\frac{\partial u}{\partial z} + i\frac{\partial v}{\partial z})$. The Brunt-Vaisala frequency N [s^{-1}] is calculated using sw_bfrq, a routine in the CSIRO SEAWATER library for MATLAB [*Morgan*, 1994] and $\hat{N}$ is N smoothed over a window equal to the segment length of the Fourier transform used in subsequent steps and subsampled to vertical resolution of $\mathbf{U}_z$.

Vertical shear and smoothed buoyancy frequency are broken into 320 m, half overlapping segments starting from the bottom of the cast, with each segment containing $M_{uz} = \frac{320m}{\Delta z_{uz}}$ points, where Δz_{uz} is the vertical resolution of the shear (typically 10 m). The unsmoothed profiles of N^2 at 1 m vertical resolution are divided into 320 m long segments that exactly overlap the segments of $\frac{\mathbf{U}_z}{\hat{N}}$. To calculate isopycnal strain,

$$\xi_z = \frac{N^2 - N^2_{fit}}{\overline{N^2}}, \tag{A1}$$

the difference is found between the unsmoothed stratification and the cubic fit of N^2, N^2_{fit}, and the quantity is normalized by the segment-averaged stratification, $\overline{N^2}$. Potential errors arise from choosing to use a cubic fit of N^2 rather than the more accurate but computationally expensive adiabatic leveling, with errors being largest in the upper ocean where stratification changes the most rapidly. To quantify the potential error associated with this choice, all 320 m segments from the top 500 m of the water column of N^2 observations and their corresponding N^2_{fit} were used to generate mean profiles of N^2 and N^2_{fit} to determine how well the fits are able to replicate the observed mean field. For these mean profiles, the N^2_{fit} is found to on average overestimate N^2 by only 0.4%. These segments are $M_{\xi_z} = \frac{320m}{\Delta z_{\xi_z}}$ points long.

The parameterization relies on relating the variance of the observed shear and strain fields to that of the theoretical Garrett-Munk (GM) wavefield, which has a well-defined wave number spectrum that is a function of local stratification and Coriolis. Thus, the Fourier transform of each segment of $\frac{\mathbf{U}_z}{\hat{N}}$ and ξ_z,

$$\Phi_{uz}(k_z) = \mathcal{F}\left(\frac{\mathbf{U}_z}{\hat{N}} * W_{uz}(k_z)\right), \tag{A2}$$

$$\Phi_{\xi z}(k_z) = \mathcal{F}(\xi_z * W_{\xi z}(k_z)), \tag{A3}$$

which is a function of vertical wave number, k_z, is taken after removing a linear fit from each segment and then convolving the physical quantity with a variance preserving window, $W(k_z) = w(k_z) \Big/ \sqrt{\frac{\sum w(k_z)^2}{M}}$, where $w(k_z)$ is an M_{uz} or $M_{\xi z}$-point Hanning window, respectively.

The spectra

$$S(k_z)=\frac{\Delta z}{2\pi M}2[\Phi_r^2(k_z)+\Phi_i^2(k_z)]S_{correc}(k_z) \tag{A4}$$

is formed from the real and imaginary Fourier coefficients, where $\Phi(k_z)=\Phi_r(k_z)+i\Phi_i(k_z)$, normalized by $\frac{\Delta z}{2\pi M}$ so that Parseval's theorem is satisfied and corrected for loss of variance due to data processing with $S_{correc}(k_z)$.

The correction term for shear spectra, $S_{uzcorrec}(k_z)$, contains terms that account for variance lost to (c1) range averaging, (c2) finite differencing, (c3) interpolation, and (c4) instrument titling, where $S_{uzcorrec}(k_z)=S_{c1}S_{c2}S_{c3}S_{c4}$. These terms are defined as,

$$S_{c1}=\mathrm{sinc}\left(\frac{k_z\Delta z_t}{2\pi}\right)^{-2}\mathrm{sinc}\left(\frac{k_z\Delta z_r}{2\pi}\right)^{-2}, \tag{A5}$$

$$S_{c2}=\mathrm{sinc}\left(\frac{k_z\Delta z}{2\pi}\right)^{-2}, \tag{A6}$$

$$S_{c3}=\mathrm{sinc}\left(\frac{k_z\Delta z_r}{2\pi}\right)^{-4}\mathrm{sinc}\left(\frac{k_z\Delta z}{2\pi}\right)^{-2}, \tag{A7}$$

$$S_{c4}=\mathrm{sinc}\left(\frac{k_z\bar{d}}{2\pi}\right)^{-2}, \tag{A8}$$

with Δz_t the LADCP transmitted vertical pulse length, Δz_r the LADCP receiver processing bin length, Δz the resolution of the data, and $\bar{d}=9$ m, determined empirically by *Polzin et al*. [2002]. The correction term for strain spectra only needs to account for the loss of variance due to first differencing, $S_{\xi zcorrec}(k_z)=\mathrm{sinc}\left(\frac{k_z\Delta z_{\xi_z}}{2\pi}\right)^{-2}$.

The spectral variance, $\langle S\rangle$, is quantified by integrating the spectra over an appropriate vertical wave number range. For the shear spectra, the minimum wave number, k_{min}, corresponds to the largest resolved wavelength which is equal to the segment length, while the maximum wave number corresponds to the smallest wavelength that is distinctive from instrument noise ($\lambda_z=50$ m) [*Polzin et al*., 2002]. If necessary, k_{max} is adjusted when the spectra is saturated such that $\langle S_{uz}\rangle \leq 0.67$. For strain spectra, k_{min} is set to limit contamination due to stratification with an equivalent wavelength of 150 m and k_{max} has a wavelength of 10 m to avoid instrument noise and is adjusted such that $\langle S_{\xi_z}\rangle \leq 0.22$ [*Kunze et al*., 2006].

The GM spectrum takes the form,

$$S_{GM}=r_{GM}\frac{\pi}{2}E_0 b j_*\frac{k_z^2}{(k_z+k_z^*)^2}, \tag{A9}$$

where $r_{GM}=3$ for the GM shear spectrum and $r_{GM}=1$ for the strain spectrum, $k_z^*=\pi j_*\bar{N}/bN_0$, b = 1300 m, $j_*=3$, $E_0=6.3\times10^{-5}$, $N_0=5.24\times10^{-3}$ rad s^{-1}, and $\bar{N}$ is the segment-averaged buoyancy frequency. For every segment of shear and strain a corresponding GM spectrum is calculated and integrated over the same wave number ranged used for integrating the observed spectra.

The observed and GM variances are used to estimate the ratio of shear to strain variance in the segment,

$$R_\omega=\frac{3\langle S_{uz}\rangle\langle S_{\xi zGM}\rangle}{\langle S_{\xi z}\rangle\langle S_{uzGM}\rangle}. \tag{A10}$$

The ratio is also a measure of the aspect ratio of the observed internal wavefield. In the Solomon Sea, we find a mean $R_\omega=4.2$.

The parameterization uses $\langle S\rangle$ and $\langle S_{GM}\rangle$ from either shear or strain to estimate the turbulent dissipation rate,

$$\epsilon=\epsilon_0\frac{\bar{N}^2}{N_0^2}h(R_\omega)j(\bar{N},f)\frac{\langle S\rangle^2}{\langle S_{GM}\rangle^2}, \tag{A11}$$

with $\epsilon_0 = 6.73 \times 10^{-10}$. Dissipation is adjusted for the local buoyancy frequency $\bar{N}$ and rotation, f, by

$$j(\bar{N}, f) = \frac{f \operatorname{arccosh}(\frac{\bar{N}}{f})}{f_{30} \operatorname{arccosh}(\frac{N_0}{f_{30}})}, \tag{A12}$$

with $f_{30} = f(30^\circ)$. An additional correction, $h(R_\omega)$, is applied and its form depends on whether the shear or stain variance is used. When using $\langle S_{uZ} \rangle$ to estimate ϵ,

$$h(R_\omega) = \frac{3(R_\omega + 1)}{2\sqrt{2R_\omega(R_\omega - 1)}}, \tag{A13}$$

and when $\langle S_{\xi z} \rangle$ is used,

$$h(R_\omega) = \frac{R_\omega(R_\omega + 1)}{6\sqrt{2(R_\omega - 1)}}. \tag{A14}$$

Our analysis uses $\langle S_{\xi z} \rangle$ and the mean Solomon Sea R_ω to calculate ϵ.

Acknowledgments

The Pandora and MoorSPICE cruises are contributions to the CLIVAR/SPICE and GEOTRACES International programs. The Pandora cruise has been co-funded by ANR (project ANR-09-BLAN-0233-01), INSU/LEFE, IRD, LEGOS, and NSF grant OCE1029487. The MoorSPICE cruise has been co-funded by NSF grant OCE1029487, ANR-09-BLAN-0233-01, and INSU/LEFE project Solwara. Pandora and MoorSPICE data can be found at http://www.obs-vlfr.fr/proof/cruises.php. MoorSPICE data can also be found through Cruise (doi:10.7284/903044). We are grateful to the crews of the R/V l'Atalante and R/V Thomas G. Thompson. We are also grateful to the engineers and scientists who carefully sampled, recorded, and treated the data. This subset of the Argo database was made freely available by the Coriolis project and programs that contribute to it (http://www.coriolis.eu.org). This publication benefited from the insightful and constructive comments of Robin Robertson and an anonymous reviewer.

References

Alford, M. H. (2001), Internal swell generation: The spatial distribution of energy flux from the wind to mixed layer near-inertial motions, *J. Phys. Oceanogr.*, *31*(8), 2359–2368.

Alford, M. H. (2003a), Redistribution of energy available for ocean mixing by long-range propagation of internal waves, *Nature*, *423*(6936), 159–162.

Alford, M. H. (2003b), Improved global maps and 54-year history of wind-work on ocean inertial motions, *Geophys. Res. Lett.*, *30*(8), 1424, doi:10.1029/2002GL016614.

Alford, M. H., and M. Whitmont (2007), Seasonal and spatial variability of near-inertial kinetic energy from historical moored velocity records, *J. Phys. Oceanogr.*, *37*(8), 2022–2037.

Alford, M. H., et al. (2011), Energy flux and dissipation in Luzon Strait: Two tales of two ridges, *J. Phys. Oceanogr.*, *41*(11), 2211–2222.

Alford, M. H., et al. (2015), The formation and fate of internal waves in the South China Sea, *Nature*, *521*(7550), 65–69.

Amante, C., and B. W. Eakins (2009), ETOPO1 1 arc-minute global relief model: procedures, data sources and analysis, NOAA Tech. Mem. NESDIS NGDC-24, Natl. Oceanic and Atmos. Admin., Boulder, Colo.

Cravatte, S., A. Ganachaud, Q.-P. Duong, W. S. Kessler, G. Eldin, and P. Dutrieux (2011), Observed circulation in the Solomon Sea from SADCP data, *Prog. Oceanogr.*, *88*(1), 116–130.

Davis, R. E., W. S. Kessler, and J. T. Sherman (2012), Gliders measure western boundary current transport from the South Pacific to the Equator, *J. Phys. Oceanogr.*, *42*(11), 2001–2013.

de Boyer Montégut, C., G. Madec, A. S. Fischer, A. Lazar, and D. Iudicone (2004), Mixed layer depth over the global ocean: An examination of profile data and a profile-based climatology, *J. Geophys. Res.*, *109*, C12003, doi:10.1029/2004JC002378.

Dillon, T. (1982), Vertical overturns: A comparison of Thorpe and Ozmidov length scales, *J. Geophys. Res.*, *87*(C12), 9601–9613.

Djath, B., J. Verron, A. Melet, L. Gourdeau, B. Barnier, and J.-M. Molines (2014), Multiscale dynamical analysis of a high-resolution numerical model simulation of the Solomon Sea circulation, *J. Geophys. Res. Oceans*, *119*, 6286–6304, doi:10.1002/2013JC009695.

Egbert, G., and R. Ray (2000), Significant dissipation of tidal energy in the deep ocean inferred from satellite altimeter data, *Nature*, *405*(6788), 775–778.

Egbert, G. D., and S. Y. Erofeeva (2002), Efficient inverse modeling of barotropic ocean tides, *J. Atmos. Oceanic Technol.*, *19*(2), 183–204.

Fine, R. A., R. Lukas, F. M. Bingham, M. J. Warner, and R. H. Gammon (1994), The western equatorial Pacific: A water mass crossroads, *J. Geophys. Res.*, *99*(C12), 25,063–25,080.

Frants, M., G. M. Damerell, S. T. Gille, K. J. Heywood, J. MacKinnon, and J. Sprintall (2013), An assessment of density-based finescale methods for estimating diapycnal diffusivity in the Southern Ocean, *J. Atmos. Oceanic Technol.*, *30*(11), 2647–2661.

Galbraith, P. S., and D. E. Kelley (1996), Identifying overturns in CTD profiles, *J. Atmos. Oceanic Technol.*, *13*(3), 688–702.

Ganachaud, A., et al. (2014), The Southwest Pacific Ocean circulation and climate experiment (SPICE), *J. Geophys. Res. Oceans*, *119*, 7660–7686, doi:10.1002/2013JC009678.

Gasparin, F., A. Ganachaud, C. Maes, F. Marin, and G. Eldin (2012), Oceanic transports through the Solomon Sea: The bend of the New Guinea Coastal Undercurrent, *Geophys. Res. Lett.*, *39*, L15608, doi:10.1029/2012GL052575.

Germineaud, C., A. Ganachaud, J. Sprintall, S. Cravatte, G. Eldin, M. S. Alberty, and E. Privat (2016), Pathways and water mass properties of the thermocline and intermediate waters in the Solomon Sea, *J. Phys. Oceanogr.*, *46*(10), 3031–3049.

Gourdeau, L., J. Verron, A. Melet, W. Kessler, F. Marin, and B. Djath (2014), Exploring the mesoscale activity in the Solomon Sea: A complementary approach with a numerical model and altimetric data, *J. Geophys. Res. Oceans*, *119*, 2290–2311, doi:10.1002/2013JC009614.

Gregg, M. (1989), Scaling turbulent dissipation in the thermocline, *J. Geophys. Res.*, *94*(C7), 9686–9698.

Grenier, M., S. Cravatte, B. Blanke, C. Menkes, A. Koch-Larrouy, F. Durand, A. Mélet, and C. Jeandel (2011), From the western boundary currents to the Pacific Equatorial Undercurrent: Modeled pathways and water mass evolutions, *J. Geophys. Res.*, *116*, C12044, doi:10.1029/2011JC007477.

Hristova, H. G., and W. S. Kessler (2012), Surface circulation in the Solomon Sea derived from Lagrangian drifter observations, *J. Phys. Oceanogr.*, *42*(3), 448–458.

Hristova, H. G., W. S. Kessler, J. C. McWilliams, and M. J. Molemaker (2014), Mesoscale variability and its seasonality in the Solomon and Coral Seas, *J. Geophys. Res. Oceans*, *119*, 4669–4687, doi:10.1002/2013JC009741.

Kashino, Y., I. Ueki, Y. Kuroda, and A. Purwandani (2007), Ocean variability north of New Guinea derived from TRITON buoy data, *J. Oceanogr.*, *63*(4), 545–559.

Kida, S., and S. Wijffels (2012), The impact of the Indonesian throughflow and tidal mixing on the summertime sea surface temperature in the western Indonesian seas, *J. Geophys. Res.*, *117*, C09007, doi:10.1029/2012JC008162.

Klymak, J. M., J. N. Moum, J. D. Nash, E. Kunze, J. B. Girton, G. S. Carter, C. M. Lee, T. B. Sanford, and M. C. Gregg (2006), An estimate of tidal energy lost to turbulence at the Hawaiian ridge, *J. Phys. Oceanogr.*, *36*(6), 1148–1164.
Klymak, J. M., R. Pinkel, and L. Rainville (2008), Direct breaking of the internal tide near topography: Kaena ridge, Hawaii, *J. Phys. Oceanogr.*, *38*(2), 380–399.
Koch-Larrouy, A., G. Madec, P. Bouruet-Aubertot, T. Gerkema, L. Bessières, and R. Molcard (2007), On the transformation of Pacific Water into Indonesian Throughflow Water by internal tidal mixing, *Geophys. Res. Lett.*, *34*, L04604, doi:10.1029/2006GL028405.
Koch-Larrouy, A., M. Lengaigne, P. Terray, G. Madec, and S. Masson (2010), Tidal mixing in the Indonesian seas and its effect on the tropical climate system, *Clim. Dyn.*, *34*(6), 891–904.
Koch-Larrouy, A., A. Atmadipoera, P. Van Beek, G. Madec, J. Aucan, F. Lyard, J. Grelet, and M. Souhaut (2015), Estimates of tidal mixing in the Indonesian archipelago from multidisciplinary indomix in-situ data, *Deep Sea Res., Part I*, *106*, 136–153.
Kunze, E., E. Firing, J. M. Hummon, T. K. Chereskin, and A. M. Thurnherr (2006), Global abyssal mixing inferred from lowered ADCP shear and CTD strain profiles, *J. Phys. Oceanogr.*, *36*(8), 1553–1576.
Levine, M. D., and T. J. Boyd (2006), Tidally forced internal waves and overturns observed on a slope: Results from home, *J. Phys. Oceanogr.*, *36*(6), 1184–1201.
Lindstrom, E., J. Butt, R. Lukas, and S. Godfrey (1990), The flow through Vitiaz Strait and St. George's Channel, Papua New Guinea, in *The Physical Oceanography of Sea Straits*, pp. 171–189, Springer, Netherlands.
Mater, B. D., S. K. Venayagamoorthy, L. St. Laurent, and J. N. Moum (2015), Biases in Thorpe-scale estimates of turbulence dissipation: Part I: Assessments from large-scale overturns in oceanographic data, *J. Phys. Oceanogr.*, *45*(10), 2497–2521.
Melet, A., L. Gourdeau, W. S. Kessler, J. Verron, and J.-M. Molines (2010a), Thermocline circulation in the Solomon Sea: A modeling study, *J. Phys. Oceanogr.*, *40*(6), 1302–1319.
Melet, A., L. Gourdeau, and J. Verron (2010b), Variability in Solomon Sea circulation derived from altimeter sea level data, *Ocean Dyn.*, *60*(4), 883–900.
Melet, A., J. Verron, L. Gourdeau, and A. Koch-Larrouy (2011), Equatorward pathways of Solomon Sea water masses and their modifications, *J. Phys. Oceanogr.*, *41*(4), 810–826.
Melet, A., S. Legg, and R. Hallberg (2016), Climatic impacts of parameterized local and remote tidal mixing, *J. Clim.*, *29*(10), 3473–3500.
Morgan, P. P. (1994), SEAWATER: A library of MATLAB computational routines for the properties of sea water: Version 1.2, *Rep. 222*, 37 p., CSIRO Mar. Lab., Australia.
Moum, J. N., A. Perlin, J. D. Nash, and M. J. McPhaden (2013), Seasonal sea surface cooling in the equatorial pacific cold tongue controlled by ocean mixing, *Nature*, *500*(7460), 64–67.
Munk, W., and C. Wunsch (1998), Abyssal recipes II: Energetics of tidal and wind mixing, *Deep Sea Res., Part I*, *45*(12), 1977–2010.
Murray, S., E. Lindstrom, J. Kindle, and E. Weeks (1995), Transport through Vitiaz Strait, *WOCE Notes*, *7*(1), 21–23.
Niwa, Y., and T. Hibiya (2014), Generation of baroclinic tide energy in a global three-dimensional numerical model with different spatial grid resolutions, *Ocean Modell.*, *80*, 59–73.
Oakey, N. (1982), Determination of the rate of dissipation of turbulent energy from simultaneous temperature and velocity shear microstructure measurements, *J. Phys. Oceanogr.*, *12*(3), 256–271.
Osborn, T. (1980), Estimates of the local rate of vertical diffusion from dissipation measurements, *J. Phys. Oceanogr.*, *10*(1), 83–89.
Peltier, W., and C. Caulfield (2003), Mixing efficiency in stratified shear flows, *Annu. Rev. Fluid Mech.*, *35*(1), 135–167.
Polzin, K., E. Kunze, J. Hummon, and E. Firing (2002), The finescale response of lowered ADCP velocity profiles, *J. Atmos. Oceanic Technol.*, *19*(2), 205–224.
Polzin, K. L., J. M. Toole, and R. W. Schmitt (1995), Finescale parameterizations of turbulent dissipation, *J. Phys. Oceanogr.*, *25*(3), 306–328.
Polzin, K. L., A. C. Naveira Garabato, T. N. Huussen, B. M. Sloyan, and S. Waterman (2014), Finescale parameterizations of turbulent dissipation, *J. Geophys. Res. Oceans*, *119*, 1383–1419, doi:10.1002/2013JC008979.
Price, J. F., and J. Yang (1998), Marginal sea overflows for climate simulations, in *Ocean Modeling and Parameterization*, pp. 155–170, Springer, Netherlands.
Qin, X., L. Menviel, A. Sen Gupta, and E. Sebille (2016), Iron sources and pathways into the Pacific Equatorial Undercurrent, *Geophys. Res. Lett.*, *43*(18), 9843–9851.
Ryan, J. P., I. Ueki, Y. Chao, H. Zhang, P. S. Polito, and F. P. Chavez (2006), Western Pacific modulation of large phytoplankton blooms in the central and eastern equatorial Pacific, *J. Geophys. Res.*, *111*, G02013, doi:10.1029/2005JG000084.
Simmons, H. L., and M. H. Alford (2012), Simulating the long-range swell of internal waves generated by ocean storms, *Oceanography*, *25*(2), 30–41.
Simmons, H. L., R. W. Hallberg, and B. K. Arbic (2004), Internal wave generation in a global baroclinic tide model, *Deep Sea Res., Part II*, *51*(25), 3043–3068.
St Laurent, L. (2008), Turbulent dissipation on the margins of the South China Sea, *Geophys. Res. Lett.*, *35*, L23615, 10.1029/2008GL035520.
St Laurent, L., H. Simmons, and S. Jayne (2002), Estimating tidally driven mixing in the deep ocean, *Geophysical Research Letters*, *29*(23), 2106, doi:10.1029/2002GL015633.
St. Laurent, L. C., J. M. Toole, and R. W. Schmitt (2001), Buoyancy forcing by turbulence above rough topography in the abyssal brazil basin, *J. Phys. Oceanogr.*, *31*(12), 3476–3495.
Thompson, A. F., S. T. Gille, J. A. MacKinnon, and J. Sprintall (2007), Spatial and temporal patterns of small-scale mixing in Drake Passage, *J. Phys. Oceanogr.*, *37*(3), 572–592.
Thorpe, S. (1977), Turbulence and mixing in a Scottish loch, *Philos. Trans. R. Soc. London A*, *286*(1334), 125–181.
Tomczak, M., and J. S. Godfrey (2013), *Regional Oceanography: An Introduction*, Elsevier, Great Britain.
Tsuchiya, M., R. Lukas, R. A. Fine, E. Firing, and E. Lindstrom (1989), Source waters of the Pacific equatorial undercurrent, *Prog. Oceanogr.*, *23*(2), 101–147.
Waterman, S., K. L. Polzin, A. C. Naveira Garabato, K. L. Sheen, and A. Forryan (2014), Suppression of internal wave breaking in the Antarctic Circumpolar Current near topography, *J. Phys. Oceanogr.*, *44*(5), 1466–1492.
Whalen, C., L. Talley, and J. MacKinnon (2012), Spatial and temporal variability of global ocean mixing inferred from Argo profiles, *Geophys. Res. Lett.*, *39*, L18612, doi:10.1029/2012GL053196.
Whalen, C. B., J. A. MacKinnon, L. D. Talley, and A. F. Waterhouse (2015), Estimating the mean diapycnal mixing using a finescale strain parameterization, *J. Phys. Oceanogr.*, *45*(4), 1174–1188.
Winkel, D. P., M. C. Gregg, and T. B. Sanford (2002), Patterns of shear and turbulence across the Florida current, *J. Phys. Oceanogr.*, *32*(11), 3269–3285.
Zilberman, N., D. Roemmich, and S. Gille (2013), The mean and the time variability of the shallow meridional overturning circulation in the tropical South Pacific Ocean, *J. Clim.*, *26*(12), 4069–4087.